Nuclear Materials and Energy 25 (2020) 100855

Contents lists available at ScienceDirect

Nuclear Materials and Energy

journal homepage: www.elsevier.com/locate/nme

Liquid metal "divertorlets" concept for fusion reactors

A.E. Fisher [a], Z. Sun [b], E. Kolemen [a,*]

[a] Department of Mechanical and Aerospace Engineering, Princeton University, Princeton, NJ, USA
[b] Princeton Plasma Physics Laboratory, 100 Stellarator Road, Princeton NJ, USA

ARTICLE INFO

Keywords:
Flowing liquid metal
Divertor
Lithium
Low-recycling
Divertorlets
High heat flux

ABSTRACT

A new, novel approach to liquid metal plasma facing components called "divertorlets" is presented and accompanied by experiments, simulations, and analysis. The development of a robust and reliable plasma facing component at the divertor is ongoing, with liquid metal divertor concepts gaining interest by showing promise for being able to handle higher heat fluxes as well as improve plasma performance through a reduction in particle recycling. The presented design in this work seeks to address challenges associated with evaporation, operation power, and liquid metal inventory. Divertorlets utilize many adjacent narrow channels with alternating vertical velocity that maintain large flow rates with small velocities at the surface by minimizing the flow path length. Preliminary results using a test stand on LMX-U at PPPL and simulations in COMSOL demonstrate the successful operation and the potential for divertorlets to remove large heat fluxes, with projections made to reactor scale showing the expected system performance.

1. Introduction

1.1. Motivation and background

Tokamak fusion reactors can experience extreme heat flux in the divertor region. Within an experimental device the divertor region may reach heat flux over 10[MW/m^2], and this number will likely become larger in a commercial device [1]. Solid divertor solutions like those proposed on ITER have shortcomings both in handling the upper limits of heat flux as well as having potential to experience irreversible damage that would require frequent shutdown and component replacement. Liquid metals are a proposed solution to address both of these challenges in their ability to actively carry away heat and self-heal through constant replenishment. Numerous liquid metal systems have been investigated for the last several decades, and beyond the details of the geometry and operation of the systems the working liquid metal is also hotly debated.

For the design considerations and calculations for the concept presented in this work the working liquid metal is lithium. Lithium offers low density, low-Z, and creates a low-recycling condition that makes it a primary candidate as an LM-PFC [2–4]. Tin is also under consideration despite being over an order of magnitude larger in both density and atomic size, but it can work under significantly higher temperatures before evaporating which provides for a larger operating regime that relaxes certain design constraints [5].

Amongst all of the factors that come into a lithium system design the three most important considerations for each concept are the following:

– Reducing the lithium inventory as much as possible
– Minimizing the amount of energy required to run the liquid metal system
– Avoiding excessive evaporation and splashing of the liquid metal

Failure in any one of these three areas effectively translates to the design being infeasible. The target goals for these areas of consideration with a new design were the following:

– Less than 200[kg] of lithium
– Less than 5% of the rated reactor power to operate
– Maintaining peak lithium temperature below 475[C] with flow speeds under 30[cm/s]

Reduction of lithium inventory requires as little lithium as possible exposed to the plasma at a time, and as little supporting plumbing as possible. Lowering the required power to operate the system can be accomplished by reducing flow speeds to minimize MHD drag losses. Finally, maintaining a low peak lithium temperature at low speeds requires the lithium to be taken in and out of the heat flux region over short distances. Divertorlets accomplish all of these tasks by having no

* Corresponding author.
E-mail address: ekolemen@pppl.gov (E. Kolemen).

https://doi.org/10.1016/j.nme.2020.100855
Received 24 July 2020; Received in revised form 6 November 2020; Accepted 17 November 2020
Available online 2 December 2020

plumbing leading out of the reactor, and having lithium travel minimal distance in the hot area to keep flow speeds low.

2. LM-PFC concepts

There are numerous LM-PFC concepts that have been proposed for the purpose of handling large amounts of heat flux from a tokamak divertor. Amongst the LM-PFC concepts there is not a consensus on which provides the best traits for a reactor setting, and the advantages and existing challenges for various designs are continuously reviewed [6–9]. A set of common weaknesses have been determined from these reviews for the benefit of future designs.

Flow speed of the liquid metal is one of the more important considerations for the designs as it greatly contributes to MHD drag. Fast-flowing concepts are most susceptible to MHD drag which often causes losses that far exceed any hydrodynamic losses, translating either to flow piling in a free-surface application or massive pressure drop within a closed duct. Slow-flowing concepts avoid MHD drag, but are then challenged with avoiding evaporation.

Another of the major concerns with LM-PFCs is droplet ejection and splashing into the plasma. While $j \times B$ force can be used in LM-PFCs for a positive effect, there are also instances where $j \times B$ force can be induced by plasma currents or magnetic field changes that result in the droplet ejection and/or splashing. These stability limits have been investigated by others and add additional design considerations [10].

Despite the projected challenges with implementation the expected benefits for reactor operation remain significant. Lithium PFCs have been tested and shown to improve plasma performance to reach higher confinement and reduce ELMs even as a monolayer coating, with further improvements expected from flowing systems that may self-heal and replenish [11–13].

2.1. Fast-flowing concepts

Fast-flowing LM-PFC concepts attempt to remove the incoming heat from the divertor region entirely by way of the flowing liquid metal while also avoiding large temperature increases that would cause the liquid metal to evaporate. The concepts accomplish protecting the substrate from thermal stress, creating a low-recycling condition that leads to a higher plasma confinement, and reduces impurity introduction into the plasma by preventing evaporation. Fast-flow can been achieved in a free-surface context with mechanisms such as the Marangoni effect and $j \times B$ force, with the latter being suitable for control in a continuous flow loop [3,14]. Fast-flowing designs are faced with criticism that MHD drag is insurmountable at the required flow speeds and are predicted to have high-risk of piling and splashing [15].

A recently designed experiment to demonstrate a fast-flowing free-surface liquid metal divertor is Flowing LIquid Torus (FLIT). This fast-flowing concept relies on $j \times B$ force to restrain and energize the flow to offset the negative effects from MHD drag, as well as oppose any $j \times B$ forces created by plasma currents. While the flow speeds are projected to avoid evaporation and the restraint may prevent splashing, the fast flowing concepts suffer in managing power consumption, and liquid metal inventory to some extent.

MHD drag creates a large pressure drop in fast flowing systems, translating to requiring significantly more power to drive. It is possible to reduce MHD drag in the pumping system through increasing lithium inventory–allowing for larger pipes in support that provide the same flow rate at a lower speed–but lithium inventory becomes more of a problem, and the MHD drag outside the plumbing is not at all affected. With the optimizations chosen for FLIT, when scaled to an ITER-sized device the power consumption would likely exceed 10% of the reactor power, and the liquid metal inventory would exceed 500[l] [16]. Conducting experiments of this nature are an essential part of optimizing the design, but the challenges are apparent.

2.2. Slow-flowing concepts

Slow-flowing LM-PFCs do not attempt to use the liquid metal flow as the primary heat removal mechanism, but instead serve as a self-healing surface with the heat conducting through the liquid metal to be removed by a cooling solution within the substrate. By having slow-flow the power requirements to operate the system are vastly reduced through the dramatic reduction of MHD drag. However, a primary challenge to slow flowing solutions is keeping the peak lithium temperature low as the slower flow does not effectively remove heat–resulting in excessive evaporation of lithium. A proposed solution to avoid this temperature rise is maintaining a thin enough layer that a steep thermal gradient is created with minimal temperature increase, resulting in both high heat flux and low surface temperatures. Although, as no heat is removed by the lithium this moves the problem by requiring the underlying solid substrate to remove the heat at operational temperatures far below those of actively cooled solid PFCs.

2.2.1. Thermoelectric Magnetohydrodynamics (TEMHD)

With the power requirements being low to circulate the liquid metal in a slow-regime, one solution under consideration is using the Seebeck effect–more commonly referred to as the thermoelectric effect [17]. The thermoelectric effect creates a voltage based on material properties and thermal gradients which then leads to an electrical current. Interaction of that electrical current with the ambient reactor magnetic field then results in a $j \times B$ force. Using the large thermal gradients present in free-surface LM-PFCs to create a flow via $j \times B$ force has been experimentally shown at small-scales like trench flows, and is a mechanism of interest to help improve the pumping in other LM-PFC concepts [18–20].

2.2.2. Capillary-pore systems (CPS)

A popular concept within the slow-flowing solutions is a capillary-pore system, or CPS. CPS works off of immersing a fine mesh in liquid lithium, with the capillary forces associated with the small length scales causing the lithium to both spread throughout the mesh as water does in a sponge, and also restrain the flow from ejecting droplets [21]. A shortcoming of CPS is the inability to prevent evaporation from the mesh surface, however the lithium that does evaporate is projected to cool the underlying liquid layer and prevent rapid evaporation [22]. Thermal stresses are eliminated by reduction of temperature gradients, and the lithium may be gradually cycled in and out of the system to address concerns of tritium retention.

2.3. In-and-out honeycomb

A concept similar in principle to that presented here is the “in-and-out honeycomb” which uses surface-normal liquid metal pipe flows with concentric supply and drainage in a honeycomb arrangement to create a constantly replenishing free-surface [23]. The in-and-out honeycomb uses a combination of alternating magnetic fields and magnetic field gradients to generate a restraining and stabilizing $j \times B$ force on the liquid metal. Additionally, unlike divertorlets the in-and-out honeycomb design uses a separate liquid metal pump and requires the associated plumbing and liquid metal inventory increase.

3. Divertorlets concept

The divertorlets design looks to maintain the low-recycling and low-evaporation conditions associated with fast-flowing liquid metal systems with a reduced flow speed that brings power requirements down. Fast-flowing systems tend to have a single inlet and outlet, and the flow must transverse the entire width of the divertor in fractions of a second to avoid evaporation [16]. Instead of having a single flow path, the divertorlets concept introduces many flow paths by positioning vertically oriented inlets and outlets as close together as possible. The benefits in the resultant flow speed are seen in (1), where l is the fixed length

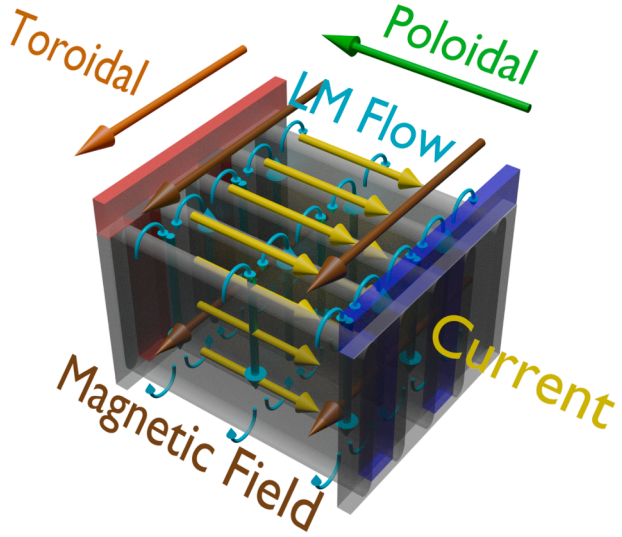

Fig. 1. 3D rendering of a small section of divertorlets with poloidally oriented slats. Not to scale.

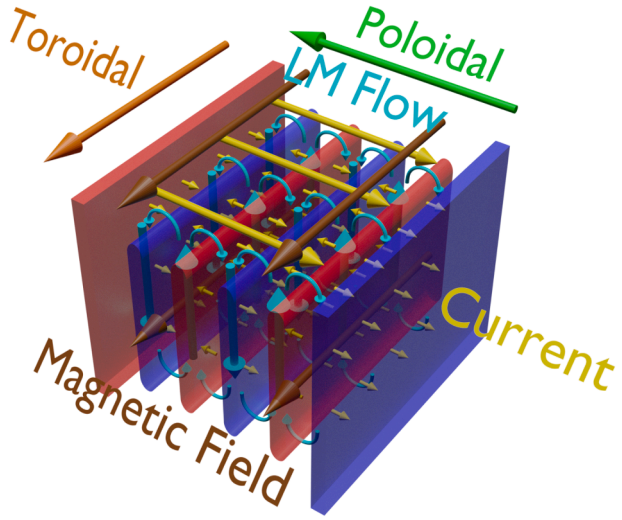

Fig. 2. 3D rendering of a small section of divertorlets with toroidally oriented slats that uses alternating polarity of slats to drive electrical currents. Not to scale.

of the liquid metal flow path, t_{cr} is the time the lithium can face the heat flux before evaporating, u is the flow speed, and N_f is the number of flow paths across the divertor length. There are several ways to calculate t_{cr} which are discussed in Section 4.2. The value of t_{cr} is constant for a given reactor condition–for lithium in a typical reactor setting t_{cr} tends to fall between 0.01[s] and 0.05[s] [16].

$$u = \frac{l}{t_{cr} N_f} \tag{1}$$

To increase the value of N_f beyond unity while keeping the divertor area covered with liquid metal, the divertorlets use directionally-alternating vertical flow paths that are connected by a single layer of liquid metal at either end–all driven by $j \times B$ force. The $j \times B$ force is generated using the ambient magnetic field within the reactor in combination with strategically placed conductors and electrodes to inject external electrical currents in a way that causes a current distribution that produces the vertically alternating flow. These alternating flow paths are separated by what will be referred to as "slats" that may be oriented radially or toroidally, with a resultant surface flow

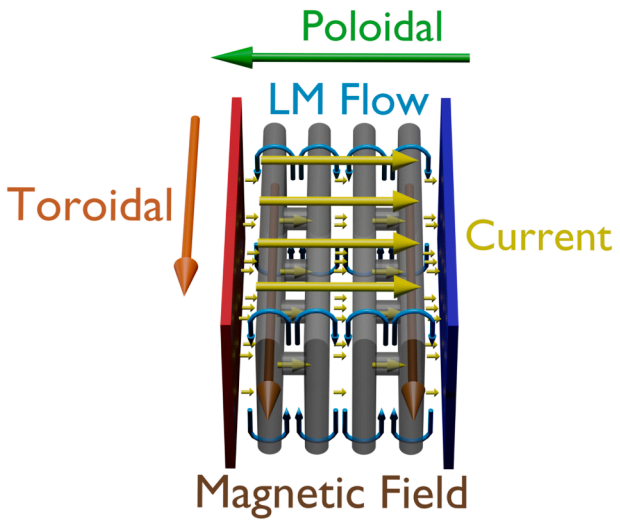

Fig. 3. 3D rendering of a small section of divertorlets with toroidally oriented slats and interconnecting rods in every-other channel to remove current from the liquid metal in those channels. Not to scale.

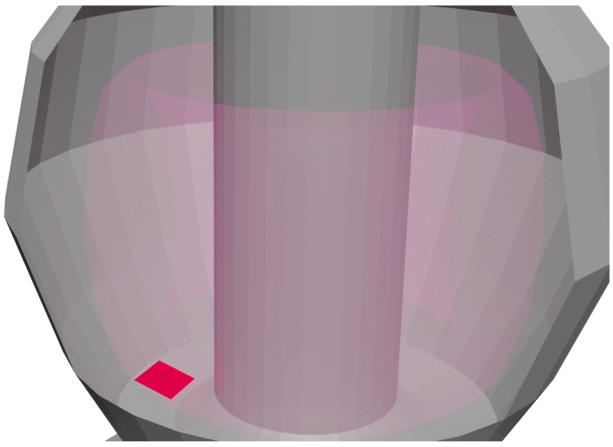

Fig. 4. Red area shows where the divertorlets depicted in Fig. 2 through Fig. 1 would be located in a reactor setting.

perpendicular to the slats. Three versions of divertorlets are shown in Figs. 1–3, with Fig. 4 showing where each is situation in the reactor divertor region. Two major classes of divertorlets are toroidal and poloidal, referring to the direction in which the slats run in the reactor.

The $j \times B$ volume force that drives the flow is shown in (2), where $\vec{j}$ is current density and $\vec{B}$ is magnetic field.

$$\vec{F}_L = \vec{j} \times \vec{B} \tag{2}$$

3.1. Poloidal divertorlets

Unlike toroidal divertorlets, poloidal divertorlets require that the slats are electrically insulated and don't act as a path for current to traverse. Accomplishing this with the slats oriented in the poloidal direction is done by placing an electrode at either-end of every-other channel as well as a surface electrode to create a restraining force. Electrical current preferentially travels in the channels that have electrodes at either end, and the concentrated $j \times B$ force results in a pressure gradient at the base of the divertorlets that generates flow.

A noted downside of poloidal divertorlets is that the expected surface waves structure tends to increase the angle at which the plasma strikes the liquid metal, although keeping wave amplitude small keep the

Table 1
Table of baseline divertorlets parameters.

Variable/Symbol	Value
Major radius: R_0	5[m]
Divertor length: L	0.2[m]
Incoming heat: Q	100[MW]
Magnetic field: B	6[T]
Coolant choice	Water @100 −200[C]avg.
Coolant density: ρ_c	9.09×10^2[kg/m^3]
Coolant viscosity: μ_c	1.824×10^{-4}[Pa s]

Table 2
Table of liquid lithium and tin parameters.

Variable/LM	Lithium [24]	Tin [25–27]
Temp. range	205 −475[C]	325 −925[C]
Avg. working temp.	340[C]	625[C]
Density	500[kg/m^3]	6722[kg/m^3]
Thermal conductivity	49.03[$\frac{W}{m \cdot K}$]	39.71[$\frac{W}{m \cdot K}$]
Electrical conductivity	3.341×10^6[S/m]	1.738×10^6[S/m]
Dynamic viscosity	5.078×10^{-4}[Pa·s]	8.618×10^{-4}[Pa·s]
Specific heat	4.169×10^3[$\frac{J}{kg\ K}$]	2.427×10^2[$\frac{J}{kg\ K}$]

increased head flux in check. Furthermore, as the current can enter channels in which it is not desired the pumping efficiency drops and flow varies across the section, however by aligning the flow profile with the heat flux profile the downside is mostly negated.

3.2. Toroidal divertorlets

Two toroidal divertorlets designs are shown in Figs. 2 and 3, to be referred as toroidal V1 and toroidal V2 respectively. The designs differ in that the former produces a current that alters in direction across the channels to produce a pumping force down and up. The latter uses a unidirectional current that causes a downwards force on the liquid metal, but that current is passed through highly-conductive structural components in every-other channel to reduce the current within the liquid metal and thus reduce the downward $j \times B$ force in those channels. This results in a net pumping force as half of the liquid metal channels experience significantly higher pressure at the base due to $j \times B$ force being higher in those channels, resulting in flow loops between the channels.

Unlike the poloidal design, the toroidal slat orientation creates an expected surface shape that does not increase plasma strike angle and maintains a lower resultant heat flux. Toroidal V1 has downsides in that it requires many electrodes and does not provide an overall-downward force on the liquid metal, resulting in loss of restraint upward-forced channel. Toroidal V2 overcomes these downsides by have a simple electrode structure as well as an overall restraining current that creates a $j \times B$ force that prevents droplet ejection.

With all of these considerations, the toroidal V2 divertorlets is considered to have the most advantages and will be the subject of further analysis in this work. It is noted however that the poloidal divertorlets have easier implemented slat cooling and a decaying flow profile that may be tuned to the decaying heat flux profile at the divertor.

4. Calculations of divertorlets parameters

The expected divertorlets operational requirements were approximated using a series of calculations to test for feasibility. As a baseline, a set of parameters for an ITER-like device are used as shown in Table 1. Considerations like coolant choice compatibility, materials, and operation conditions are not fully addressed in this work and the proposed baseline parameters are just that: baselines.

The necessary lithium inventory can be determined from the divertorlets geometry, while the divertorlets geometry is driven by factors such as: cooling requirements, $j \times B$ pumping efficiency (to be referred to as $\eta_{j \times B}$), and surface temperature considerations. Several simplifying assumptions and geometric approximations are made to capture the major scaling trends of how various dimensions effect the liquid metal inventory. To illustrate some of the differences in using lithium vs. tin from an operational standpoint, the material properties are made available in Table 2.

4.1. Liquid metal inventory

The overall volume of liquid metal was divided into three distinct sections: the liquid metal above the slats, the liquid within the channels between the slats, and the liquid metal beneath the channels. Total volume V_{tot} can be calculated with (3), where h_1 represents the thickness of the liquid metal layer from the top of the slats to the free-surface, h_2 represents the slat height, h_3 represents the thickness of the liquid metal layer from the base to the bottom of the slats, $L$is the poloidal length of the divertor, and R_0 is the radius at which the divertorlets begin. To account for the volume taken up by the slats the variable f_{ch} is introduced and represents the fraction of that region that is liquid metal depending on the width of the channels and slats (denoted by subscripts of *ch*or *s*respectively)–that calculation is shown in (4).

$$V_{tot} = V_{surf} + V_{ch} + V_{base} = \pi((R_0 + L)^2 - R_0^2)(h_1 + f_{ch}h_2 + h_3) \tag{3}$$

$$f_{ch} = \frac{w_{ch}}{w_{ch} + ws} \tag{4}$$

Given that the poloidal length of the divertorlets L is small compared to the radius at which they start, the equation can be simplified to (5).

$$V_{tot} \approx 2\pi R_0 L(h_1 + f_{ch}h_2 + h_3) \tag{5}$$

The magnitude of h_2 is expected to be significantly larger than h_1 and h_2, making keeping both h_2 and f_{ch} as small as possible particularly important in inventory reduction. Further, the poloidal length should not be made any longer than necessary.

4.2. Flow and cooling requirements

Keeping the surface liquid metal from evaporating is a hard requirement for a non-evaporative divertor design. Accomplishing that is done by both minimizing liquid metal exposure time and mixing the flow as well as possible to spread the heat out. Without any mixing heat transfer through the flow can be modeled as purely conductive heat transfer, while with perfect mixing a simple zero-dimensional heat removal method can be used. Thus, for an allowable temperature change of ΔT under an incoming heat flux $\dot{q}$–with thermal conductivity k, mass density ρ, and specific heat c_p–the two bounds that may be looked to are: one, treating the surface fluid layer and underlying slats/channels as a semi-infinite solid plate that purely conducts heat downwards (6), and two, having the surface fluid layer immediately reach a homogeneous state through perfect mixing (7). These two values of t_{cr} represent "critical times"–the amount of time that the liquid metal may be with the heated zone before reaching excessive evaporation.

$$t_{cr} = (\frac{\Delta T}{2\dot{q}})^2 \pi k \rho c_p \tag{6}$$

$$t_{cr} = \frac{\rho c_p \Delta T h_1}{\dot{q}} \tag{7}$$

As the surface layer of the divertorlets becomes thinner the semi-infinite solution becomes invalid, and the time constant is over-estimated several-fold as the actual "semi-infinite" substrate is the flow

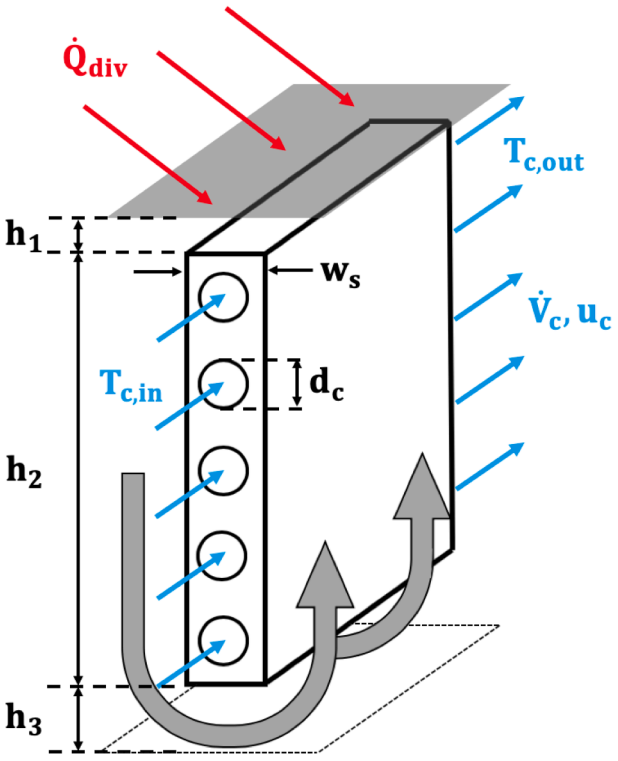

Fig. 5. Schematic of a divertorlets slat showing dimensions and cooling paths. Not to scale or representative of actual design shape and/or cooling configuration.

traveling upwards and then downwards, causing the liquid metal to be additionally heated both before and after reaching the surface layer which effectively reduces the allowable ΔT. The convective limit is similarly unrealistic as it requires instant redistribution of the heat and no peaks. Still, these critical-time values in combination with the divertorlets size provide a useful guiding estimate for what flow speed is necessary using (1).

To minimize the liquid metal inventory requirements associated with running the liquid metal through an external heat exchanger, the cooling is instead accomplished at the base of the divertorlets with additional cooling potentially possible within the slats. Cooling through the slats may be accomplished with internal cooling channels. Fig. 5 shows a summary of cooling taking place within a single slat (the exact geometry of that cooling arrangement depends on the divertorlets design). Analysis of such a setup shows the feasibility of the concept, however this analysis does not offer final design parameters as there are many additional considerations beyond the scope of this work.

A simple zero-dimensional energy balance shown in (8) estimates for the flow rate requirements for the coolant–the subscript $c$indicates a coolant property. The coolant property ΔT_c can be estimated through the expected working temperature of the liquid metal to obtain the initial guess for flow rate, and then solved for in later calculations.

$$\dot{V}_c = \frac{\dot{Q}}{c_{p,c}\rho_c \Delta T_c} \tag{8}$$

Before the heat can be carried away by the cooling fluid the heat from the liquid metal has to conduct through the slat to the cooling fluid–this heat transfer determines the temperature that the cooling fluid will exchange with. Heat conduction through the slats is governed by (9) where $\dot{Q}_s$ is the total heat flow (equal to $\dot{Q}_{div}$ for steady-state operation), k_s is the thermal conductivity of the slat material, T_f is temperature of the liquid metal, $T_{c,w}$ is the temperature of the coolant pipe wall, t_s is the effective slat wall thickness between the liquid metal and cooling fluid, and S_s is the surface area of the slat faces approximated with (11). Slat surface area increases with the number of slats N_s, the slat count is calculated with (10)-these values are for toroidal divertorlets, but the calculation approach is similar for poloidal.

$$\dot{Q}_s = k_s S_s (T_f - T_{c,w}) \Big/ t_s \tag{9}$$

$$N_s = \frac{L}{w_{ch} + w_s} \tag{10}$$

$$S_s = 4\pi N_s h_2 R_0 \tag{11}$$

Re-arranging (9) to solve for coolant pipe wall temperature results in (12).

$$T_{c,w} = T_f - \frac{t_s \dot{Q}_s}{k_s S_s} \tag{12}$$

Heat transfer into the coolant can be calculated using the convective heat transfer Eq. (13) in conjunction with (14) to find the pipe surface area A_c over which the heat is exchanged, where d_c is the cooling pipe diameter.

$$\dot{Q}_c = h_c S_c (T_{c,w} - T_{c,avg}) \tag{13}$$

$$S_c = 2N_c \pi^2 d_c R_0 \tag{14}$$

The convective heat transfer coefficient of the coolant flow h_c is found using the definition of Nusselt number shown in (15), with the Nusselt number calculated using the Dittus-Boelter relation for a heated pipe shown in (16). Values for the Reynolds number and Prandtl number are found as $\mathrm{Re}_c = \frac{\rho u_c d_c}{\mu}$ and $\mathrm{Pr}_c = \frac{c_{p,c}\mu_c}{k_c}$ respectively.

$$\mathrm{Nu} = \frac{hD}{k} \rightarrow h_c = \frac{k_c \mathrm{Nu}_c}{d_c} \tag{15}$$

$$\mathrm{Nu}_c = 0.023 \mathrm{Re}_c^{0.8} \mathrm{Pr}_c^{0.4} \tag{16}$$

Pressure drop Δp within the cooling tubes is calculated with the Darcy–Weisbach Eq. (17) using a Darcy friction factor f_D for turbulent flow in a smooth pipe. Determining the flow speed for this calculation is done by taking the calculated coolant flow Q_c and dividing it by both the cross sectional area of a coolant pipe as well as the number of coolant pipes, shown in (18) and (19).

$$\Delta p = l f_D \frac{\rho}{2} \frac{u^2}{d_c} \tag{17}$$

$$u_c = \frac{\dot{V}}{N_c \pi d_c^2 / 4} \tag{18}$$

$$N_c = N_s \frac{h_2}{2(d_c + t_w)} \tag{19}$$

Lastly, the power requirements for the coolant pumping system are determined using (20), where η_p is the pump efficiency.

$$P_c = \frac{\Delta p \dot{V}_c}{\eta_p} \tag{20}$$

Cooling accomplished at the base of the divertorlets can be accounted for using the same set of equations as the slats with a re-calculated number of cooling paths $N_{c,base}$. The geometric requirements for the base aren't as restrictive as for the slat, allowing for a more aggressive cooling solution. With all of the above equations and using the baseline parameters in Table 1 with a 5[mm] slat and channel width, slat height of 5[cm], and cooling pipes of 2.5[mm] diameter, the predicted coolant flow speed is 2.4[m/s] with a pressure drop of 2.2[atm]. Water is recognized to have prohibitive safety concerns in a liquid lithium system and is used here as an example that is well understood.

Helium cooling is an active research area in fusion engineering and standard limits of such a system are not yet agreed upon to use as scaling analysis at this point [28].

4.3. Voltage, electrical current, and power requirements

For large magnetic fields and associated large Hartmann numbers the operating power requirement is almost completely governed by the MHD drag incurred in moving the liquid metal within the reactor magnetic field, and the losses associated with viscosity may be ignored. Both the power loss *per volume* due to MHD drag and the magnitude of MHD drag are shown in (21). The value C_M is a constant that reflects how MHD drag may be mitigated by certain conditions. A C_M value of 1 would reflect the theoretical maximum drag force that could be experienced, while a value of 0 would imply no MHD drag. The effects of duct dimensions, wall conductivities, and other contributing factors to C_M have been investigated in past work [29,30].

$$P_D \propto \vec{u} \cdot \vec{F}_D \propto \vec{u} \cdot (C_M \sigma (\vec{u} \times \vec{B}) \times \vec{B}) \tag{21}$$

To determine the total power requirement the expression for power in (21) can be integrated over the volume of the liquid metal in the divertorlets. This operation is simplified by recognizing that the flow around each slat is identical, and the sum of the power requirements of each of those flows equates to the whole. Calculating the requirements of each slat can be done with a useful realization that integrating over the volume by moving along the flow path around a slat greatly simplifies the equation as the integral of the velocity across the cross section is a constant volumetric flow rate (velocity is held constant as the flow cross section is unchanged as the liquid metal moves around the slat). Then, the sum of the integration around each individual slat yields to total volumetric flow rate of the system which is determined by heat removal calculations. In consideration of the length of the flow path, the relatively small vertical components at the surface and base are ignored for simplicity and the length of the flow path is set to $2(h_2 + w_s + w_{ch})$. Additionally, we recognize that the velocity is always perpendicular to the magnetic field such that the dot and cross products can be dropped. This integration and summation yields the total power requirement scaling shown in (22).

$$P_D \propto 2(h_2 + w_s + w_{ch}) C_M \dot{V} \sigma u B^2 \tag{22}$$

Both the flow rate and velocity are present in (22), highlighting that it is more advantageous to increase flow rate by holding velocity constant while increasing flow cross section than it is to simply increase the velocity. The flow rate requirement $\dot{V}$ emerges from what is required of the liquid lithium to remove heat from the system as found in Section 4.2, the velocity is then determined through an optimization on factors such as lithium inventory and power requirements.

For the purpose of calculating $j \times B$ pumping requirements, the pressure drop expected from MHD drag (the drag force multiplied by flow path length) can be equated to the pressure created by the $j \times B$ pumping (the force-per-length across the channel width due to the *total* current, divided by the toroidal length of the channel to find pressure). An efficiency correction factor is added to account for electrical current that isn't captured by the conductive rods and opposes the pumping force. The resulting balance is shown in (23).

$$\eta_{j \times B} \frac{I}{2\pi R_0} B = 2(h_2 + w_s + w_{ch}) C_M \sigma u B^2 \tag{23}$$

Re-arranging this result as shown in (24) provides a solution for the total current required to achieve necessary pumping.

$$I = \frac{4\pi R_0 (h_2 + w_s + w_{ch}) C_M \sigma u B}{\eta_{j \times B}} \tag{24}$$

From this electrical current, the power loss P_{sys} from Ohmic heating can be found with knowledge of the resistance R_{sys} of the system. That power loss in combination with the losses due to MHD drag determine the total power as shown in (25), and the voltage V_E to drive the system can then be calculated as well.

$$P_{sys} = V_E I = I^2 R_{sys} + 2(h_2 + w_s + w_{ch}) C_M \dot{V} \sigma u B^2 \tag{25}$$

4.4. Scaling, constraints, and projections

4.4.1. Scaling

The scaling of the quantities of interest (LM inventory, surface speed, and operation power) are primarily driven by the slat height, poloidal length, and slat/channel widths (for simplicity: $w = w_s + w_c h$). Previously shown equations can be simplified to reflect the major scaling to clearly lay out the major design considerations.

Liquid metal inventory as calculated in (5) can be reduced to a simple scaling law only considering the parameters of interest as shown in (26). It can be seen that aside from reducing the footprint as much as possible, widening the slats while holding channel width constant also works to decrease the liquid metal inventory from (4).

$$V \propto L f_{ch} h_2 \tag{26}$$

Moving to surface speed, the contributions from geometry are not quite as simple. The straight-forward speed result comes from (1) in conjunction with either (6) or (7). Being able to spread the heat over a larger area reduces heat flux $\dot{q}$ in either equation while requiring a proportional increase in poloidal length L. Expressing the scaling of the surface speed in terms of slat height, channel/slat width, and poloidal length is then given by (27) and (28)–if the limiting peak heat flux cannot be reduced through an increase in L then that dependence is removed. In most current reactor environments increasing L is not expected to reduce the surface speed.

$$u_{surf} \propto \frac{w}{L^2} \rightarrow u_{surf} \propto w \tag{27}$$

$$u_{surf} \propto \frac{w}{L} \rightarrow u_{surf} \propto w \tag{28}$$

Lastly, consideration is given to scaling of the power requirements to run the system. For the sake of simplification, an assumption of $w \ll h_2$ is used to reduce the number of terms that appear in the scaling. Due to there being two terms in (25), the scaling of the losses associated with Ohmic heating in the electrical system and the losses from MHD drag are considered separately in (29) and (30). Without regards for the relative magnitude of each term, it is clear that reduction of slat size and spacing work to lower power consumption.

$$P_{Ohm} \propto h_2^2 w^2 \tag{29}$$

$$P_{MHD} \propto h_2 w \tag{30}$$

Summarizing the results, it is clear that shrinking each parameter works to improve the design in some way (except for an increase in f_{ch} through only reducing slat width leading to larger inventory)–as such, the lower-limits of these parameters need to be examined.

4.4.2. Constraints

Each of the parameters used within the aforementioned scaling laws have constraints. Some of the constraints stem from particular design considerations, for example whether or not and what kind of a coolant is to be present within the slats. For considerations of manufacturability and structural integrity, initial estimates are made but a full analysis is not offered.

Beginning with slat height, constraints arise from the necessary geometry to have the pumping and circulation properly function. For proper pumping function the slat height is estimated to need to be at least five times that of the channel-plus-slat width to keep the current in the proper area.

If the slats cool the system, they must also be sufficiently tall to

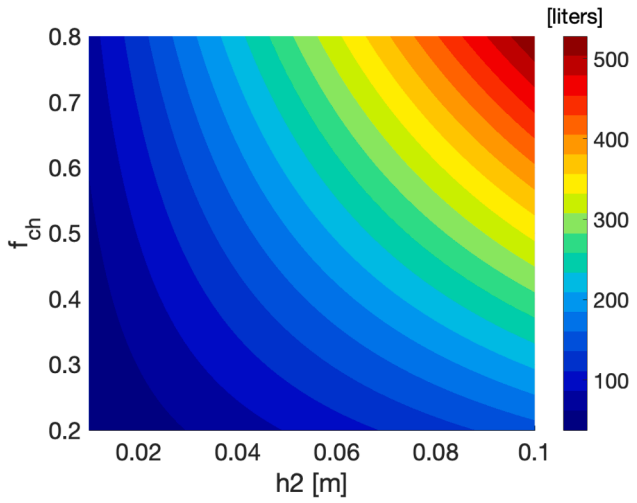

Fig. 6. Projection of lithium inventory based on the channel/slat size and slat height.

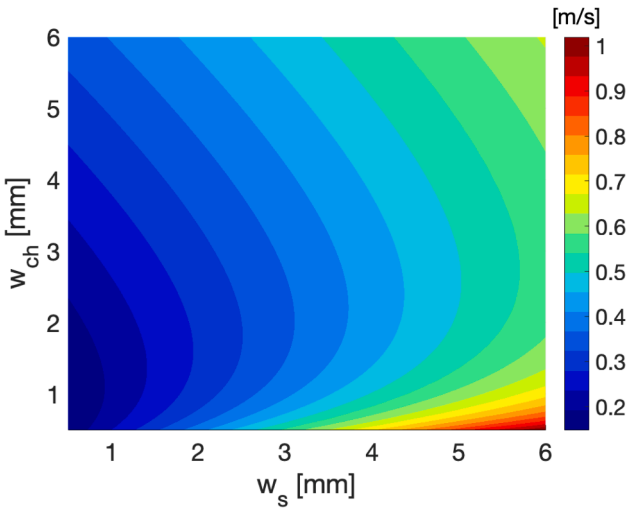

Fig. 7. Projection of flow speed based on the channel width and slat width.

accommodate the pipes. The incoming heat to the divertor per-slat $\frac{\dot{Q}_{div}}{\text{slat}}$ must be handled by some kind of heat removal system at steady-state operation, with contributions coming from the base and the slat. By working on a per-slat basis the heat is normalized by the dimensions of the footprint, so only slat height being out-of-plane contributes to heat removal, this is shown in (31) where $\dot{q}_s$ represents the heat that may be removed through a slat per-height.

$$\frac{\dot{Q}_{div}}{\text{slat}} = \frac{\dot{Q}_b + \dot{Q}_s}{\text{slat}} = \frac{\dot{Q}_b}{\text{slat}} + \frac{\dot{q}_s}{\text{slat}} h_2 \tag{31}$$

Poloidal length of the divertorlets is set based on the width at which the plasma deposits heat on the divertor. In general it is advantageous to spread this heat as much as possible to lower the peak heat flux, and the poloidal length of the divertorlets should conform to that size.

Finally, the width of both the slats and channels are constrained on hydrodynamic, structural, and cooling concerns. For the width of a slat, a minimum width may be necessitated by the presence of a cooling channel with a prescribed pipe diameter and wall thickness for operation. Without cooling, the slat still cannot be made so thin that it becomes overly fragile to the forces from the flow and $j \times B$.

Channel width on the other hand may not become so small that clogging events due to impurity formation becomes a concern. Additionally, a constraint arises from the aim to keep the surface depth close to half the channel width to maintain a constant flow cross section. As channel width and surface depth decrease the heat-removing cross section at the surface decreases as well, requiring an increase in velocity to maintain flow rate which may be prohibitive.

4.4.3. Projections

As stated from the outset, the three parameters of most interest are: the liquid metal inventory, the operational power requirements, and surface flow speed. With previously formulated equations and scaling, projections can be made for a reactor design. To better visualize the performance space, the divertorlets poloidal length will be fixed as listed in Table 1 as it only acts to linearly increase liquid metal inventory and that can be found easily.

First, projections are made for the liquid metal inventory. To reduce complexity and provide a general guide, the surface and base depth will be held constant at 2[mm] while both h_2 and f_{ch} are varied–in reality the surface depth and base depth are best set to half the channel width (which increases with f_{ch} if the slats are held constant). The expected volume of the liquid metal inventory according to (5) is shown in Fig. 6. Staying in the lower-left quadrant is ideal, although the NW/SE corners present acceptable values as well. On the other end, requiring both small

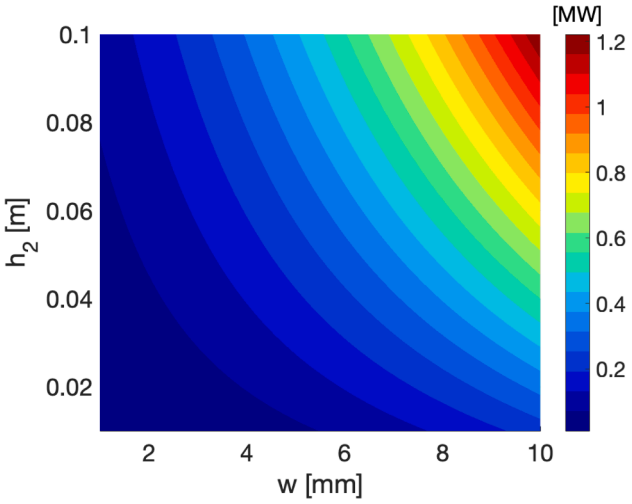

Fig. 8. Projection of the power needed to run the system–the total width is varied while holding the channel and slat widths equal according to: $w = 2w_s = 2w_{ch}$.

slats relative to flow paths and tall slats leads to prohibitively high volumes to be avoided.

Projections of surface speed are made based on the primary driving factors concluded in (27) and (28)–the slat width and channel width. Calculations for surface speed are done by dividing the transverse flow path length ($l = w_s + w_{ch}$) by the expected time that the flow can be heated. As previously discussed there are two times to consider calculated in (6) and (7)–as a first order approximation, these times are averaged and then doubled. This approach is taken to account for considerations from both timescale calculations, and make up for the underestimation at the conductive limit due to the upward flow being a worse condition that a solid plate, and the convective limit requiring unrealistic thermal mixing.

Additionally, the flow condition of having the surface depth be half the channel width is enforced in the projection. The velocity projection is shown in Fig. 7, and clearly reveals the benefits of keeping both channels and slats small.

Increasing channel width shows a relatively weak increase in surface speed compared to increasing slat width. This is due to how holding slat width constant while increasing channel width effectively increases the flow rate at the same flow speed–leading to a lower speed requirement

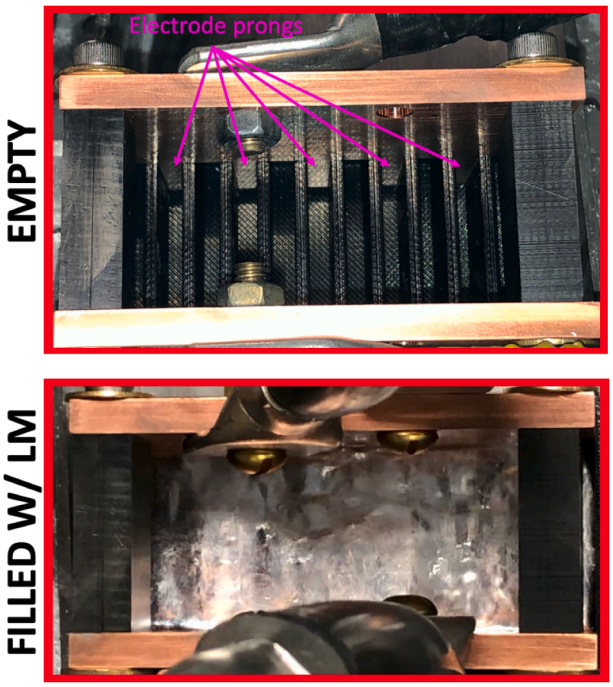

Fig. 9. An image of the poloidal divertorlets setup showing electrode prongs in every-other channel, as well as the divertorlets filled with liquid metal.

to carry the heat away. If slats carry coolant and thereby require higher thicknesses (> 3[mm]), a significantly higher flow speed will be necessary to prevent excessive evaporation.

Finally, the system power requirements are examined. As found in (30) the variables of impact are the channel/slat width and slat height, and the effect on power is shown in Fig. 8 with the bulk of operation conditions falling below 1[MW]. The power losses incurred from running the electrical current from the power supply to the divertorlets are not included in the figure. While these losses are important we do not include them as it will heavily depend on the machine and type of connections–the losses can be substantial, with some designs finding effective efficiencies of less than 20% [16].

Operations in the SW quadrant with small geometry keeps power requirements negligible compared to the reactor power, while increasing geometric scales quickly raises the power requirements.

Overall, the clear direction to take the design is to reduce the system dimensions as much as possible. Both slat height and channel/slat width have strong effects on two-out-of-three design considerations, and given that each of these parameters are constrained in the slat-cooling case it would seem to be beneficial to stay in the non-cooled slat regime and have the cooling handled at the base.

5. Poloidal divertorlets experiment

5.1. Experimental setup

Experiments were performed on a poloidal divertorlets test section using the LMX-U facility at PPPL. Unlike the toroidal divertorlets, poloidal divertorlets must be fully electrically insulated and can be 3D printed in plastic.

The divertorlets structure used had twelve slats having a height and width of 28[mm] and 3[mm] respectively, channel width of 5[mm], and bottom gap of 6[mm]. A $1/4''$ thick copper "comb" was inserted at either end that had prongs that entered every-other divertorlets channel to the base of the slats. Each copper comb was connected to a power supply with two connection points on the copper comb to better distribute current across the comb. The working fluid was a 67% Ga, 20.5% In, 12.5% Sn eutectic alloy that is commonly referred to as "galinstan".

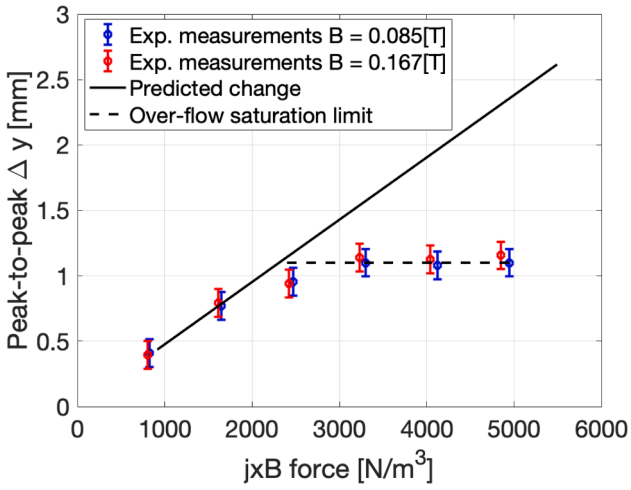

Fig. 10. Depth change at various $j \times B$ configurations–the predicted depth change assumed there was no over-flow preventing the depth change from further increasing, while the saturation limit represents when flow spilled over the slats.

The divertorlets setup was placed within the LMX-U magnet and operated up at various field strengths–characterization of the magnetic field can be found in past work [14,31]. Current up to 700[A] was able to be injected through the liquid metal using a Magna-Power TSA16-900/480 + LXI DC power supply. A Sony Cyber-Shot RX10 IV was used to take images and video up to 1000 frames per second of the divertorlets surface. Fig. 9 shows an image of the divertorlets both empty and full of galinstan within the LMX-U channel. The electrode prongs are seen in every-other channel–the same prong structure is on the other end of the divertorlets.

Direct flow speed measurements of the liquid metal within a channel during steady-state operation was infeasible due to the small length scales prohibiting certain traditional in situ measurement devices, material-related incompatibilities with galinstan (corrosivity, high electrical conductivity, etc.), and the opaqueness prohibiting optical techniques. Surface particle tracking was attempted, but as has been observed in past experiments the surface impurities on galinstan flows can remain stationary on top of a flow below a certain threshold [32]. During operation there was a substantial amount of surface deformation and apparent flow taking place of order centimeters per second, but a meaningful and measurable net motion of surface particles could not be made.

In order to get an idea of the pumping pressure within the channel without being able to take a direct measurement the divertorlets were purposefully drained to have the liquid metal rest below the top of the slats such that the $j \times B$ pumping force would cause a visible change in depth across the channels.

5.2. Experimental results

Video of a colored surface particle on the surface of an upward-forced channel was translated to a displacement using pixel tracking techniques, similar to past methods on LMX-U that tracked small changes in laser sheet height [33]. Due to the current spreading throughout channels, the $j \times B$ force considered is the difference in force between the channels with and without electrodes, as it is that resultant pressure difference that results in depth change. A plot of the particle displacement at various $j \times B$ forces is shown in Fig. 10, with the same forces used at two different magnetic fields to verify that there was no independent dependence on magnetic field or electrical current.

The "predicted change" curve is based off of a hydrostatic calculation with an efficiency correction factor where the pressure at the base of the

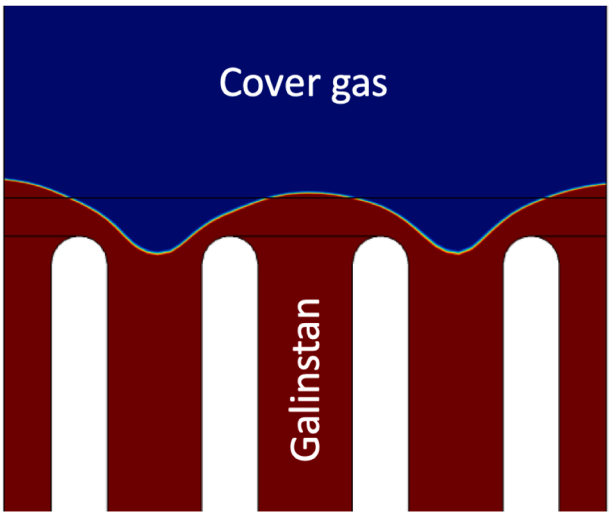

Fig. 11. Predicted surface shape of LMX-U experiment, the dividing line between the fluids represents the 0.5 volume fraction crossover from the simulation.

slats is in equilibrium, and does not account for galinstan beginning to spill over into adjacent channels which leads to the saturation limit. The pressure balance of an electrode channel (subscript a) and non-electrode channel (subscript b) is shown in (32), where Δh is the change of depth from the baseline depth (conservation of mass requires that $-\Delta h_a = \Delta h_b$). The correction factor necessary to fit the data suggests the current distribution was roughly 70% of the total within the electrode channels and the remaining 30% moved into the non-electrode channels–resulting in a pressure drop less than half of what would be the theoretical maximum for the given $j \times B$.

$$(\eta_{j\times B} j \times B + \rho g) h_a = \rho g h_b \rightarrow \eta_{j\times B} j \times B h_a = \rho g (2\Delta h) \tag{32}$$

At $j \times B \approx 2000[\mathrm{N/m^3}]$ the liquid metal within the non-electrode channel raised above the slats and galinstan began to spill over. Further projected change in depth based on hydrostatics is not realized at the tracer particle point due to the overflow draining into the adjacent channels. Using the projection however, the pressure head can be predicted by doubling the value of the black curve (the value is doubled due to an increase in depth in one channel resulting in an equal decrease in another).

6. Simulation

Simulations of the divertorlets were done with COMSOL 5.4 using the CFD module, AC/DC module, and heat transfer capabilities [34–36].

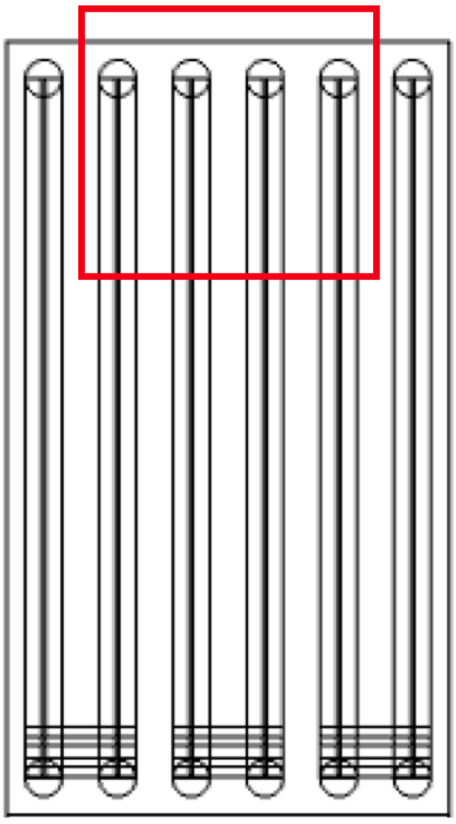

Fig. 13. Entire simulation domain for toroidal divertorlets containing interconnecting rods at the base. The area outlined in red is the portion shown in the results to highlight the area of interest.

Both a simulation of a poloidal divertorlets setup similar to the one used at LMX-U and a simulation of toroidal V2 divertorlets were performed. The poloidal case was done to work as an approximation to the experiment done on LMX and employed the level set method described in general by others and in COMSOL documentation to resolve the free-surface, while the toroidal case was done to demonstrate handling of high heat fluxes and did not employ a free-surface [37,34].

The simulation domain employed no-slip boundary conditions on all physical surfaces and had slip boundaries in the poloidal case where a boundary occurs in the middle of a channel. Electrical currents were created by applying a difference in electric potential boundary condition on electrode surfaces. Simulation boundaries were otherwise treated as electrically and thermally insulating. All appropriate material properties are applied to components within the domain, however the slats in the

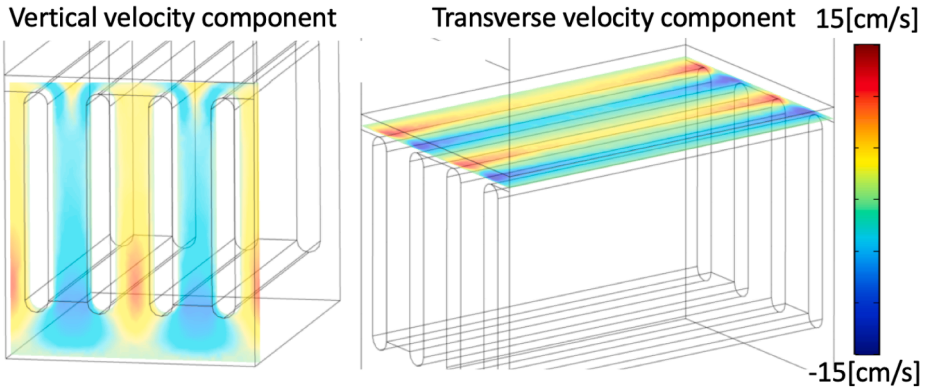

Fig. 12. Color represents velocity, with the same scale used for the vertical and transverse plots–red implies flow in the positive direction, while blue is in the negative direction.

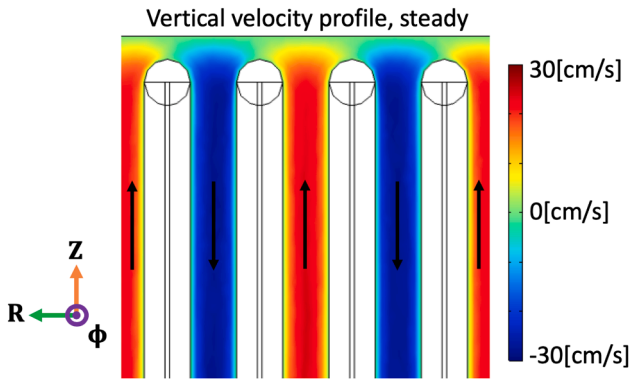

Fig. 14. Vertical velocity profile of the toroidal v2 setup, with red indicated upward flow and blue indicating downward flow.

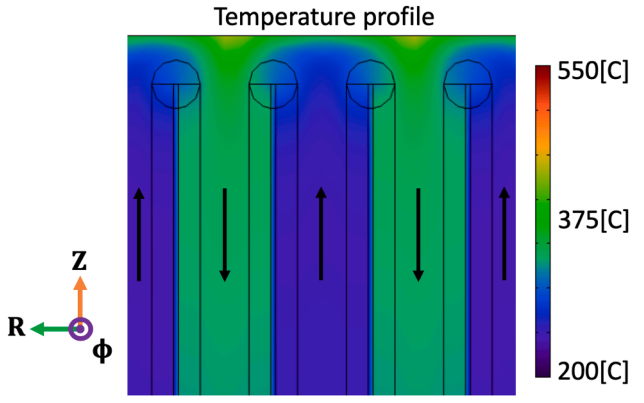

Fig. 15. Temperature profile of the toroidal v2 setup with cooled lithium traveling upwards and heated lithium being drawn downwards.

poloidal simulation are treated as voids as they carry neither current nor heat. At this point the effects of plasma pressure on the flow surface and any resulting instabilities have not been considered.

6.1. Poloidal divertorlets simulation

An LMX-like poloidal divertorlets setup was simulated. The geometry was made to represent an LMX-like setup with slat width of 3[mm], channel width of 5[mm], and 50[mm] length–the domain was restricted to two channels with electrodes, and one and two half channels without electrodes (the two half channels are at either end of the domain). The interpolated free-surface shape at the edge of the domain next to the electrode is shown in Fig. 11. Qualitative comparison to the experiments done showed surface displacements of similar size.

The vertical velocity profile towards the edge of the section as well as the transverse velocity at the surface is shown in Fig. 12. The surface flow speed is seen to decrease towards the middle of the divertorlets as pumping efficiency drops due to the spreading current–however, the exponential heat flux profile typically experienced at the divertor may be matched to this such that the highest heat flux is handled by the fastest flow, and the lower heat flux may be handled by the slower flow.

6.2. Toroidal divertorlets simulation results

A toroidal divertorlets setup using interconnecting conducting rods between channels was also performed using COMSOL. Slats and channels were set to be 1[mm] wide and 20[mm] high, with the surface layer kept to 0.5[mm] deep–the surface was kept flat as an approximation. As previously described, the interconnecting rods within every-other channel are significantly more conductive than the liquid metal and essentially remove all current from the liquid metal in the channels they pass through. Variance in current density across the channels leads to $j \times B$ gradients that lead to pumping at the bottom of the slats, with Fig. 13 showing the simulation domain with the interconnecting rods shown towards the bottom (the interconnecting rods are out-of-plane).

A 10[MW/m^2] heat flux was added to the surface of the setup to quantify how heat is removed from the surface to maintain an acceptable peak temperature and avoid evaporation. Each of the slats in the simulation contain a 0.1[mm] slit that thermally (and electrically) insulates the adjacent channels to prevent heat from transferring across–this could be similarly accomplished with cooling channels. An example of the vertical velocity profile and temperature profile for one such simulation are shown in Figs. 14 and 15

The flow configuration shown is able to maintain a peak surface temperature 450[C] occurring at "hot-spots" above the channels that flow downwards. Initial lithium temperature was set to 225[C], as the hot lithium was re-circulated the temperature gradually rose–for an actual system implementation this heat would have to be removed at the base. The flow field was created through pumping via $j \times B$ using electrodes at either end of the domain. Simulations were run up to magnetic fields of 0.3[T], matching the maximum magnetic field that may be used for future experiments on LMX-U.

7. Summary and outlook

This work illustrates that divertorlets have the potential to serve as a non-evaporative liquid metal solution for heat removal and low-recycling regime operation. Initial experiments demonstrated successful operation of a divertorlets configuration, with accompanying simulations showing the ability to handle high heat flux. By operating with many of the traditional advantages of fast- and slow-flowing solutions and having addressed many of the disadvantages, divertorlets have more potential in a reactor implementation than many of the alternatives.

The toroidal V2 configuration of divertorlets is viewed as the one with the most potential and will be the primary focus of future work. An experimental setup is planned to perform experiments like the poloidal setup shown in this work, with the inclusion of heat flux to provide another method of measurement. Flow measurements will be a high priority for future experiments to more clearly demonstrate the flow rather than rely solely on simulation results. However, expansion of the simulations is planned with aims to implement and project the performance of various cooling solutions as well as operation at higher magnetic field conditions.

Declaration of Competing Interest

The authors declare that they have no known competing financial interests or personal relationships that could have appeared to influence the work reported in this paper.

Acknowledgments

This work was supported by the United States Department of Energy through Field Work Proposal No. 1019, Domestic Liquid Metal Plasma Facing Component Development.

The research described in this paper was conducted under the Laboratory Directed Research and Development (LDRD) Program at Princeton Plasma Physics Laboratory, a national laboratory operated by Princeton University for the U.S. Department of Energy under Prime Contract No. DE-AC02-09CH11466.

This manuscript is based upon work supported by the U.S. Department of Energy, Office of Science, Office of Fusion Energy Sciences, and has been authored by Princeton University under Contract No. DE-AC02-09CH11466 with the U.S. Department of Energy.

The publisher, by accepting the article for publication, acknowledges that the United States Government retains a non-exclusive, paid-up,

irrevocable, worldwide license to publish or reproduce the published form of this manuscript, or allow others to do so, for United States Government purposes.

Digital data for this paper can be found at: http://arks.princeton.edu/ark:/88435/dsp01x920g025r.

References

[1] ITER Physics Expert Group on Divertor, Iter physics basis chapter 4: power and particle control, Nucl. Fusion 39 (1999) 2391.

[2] V.A. Evtikhin, I.E. Lyublinski, A.V. Vertkov, S.V. Mirnov, V.B. Lazarev, N. P. Petrova, S.M. Sotnikov, A.P. Chernobai, B.I. Khripunov, V.B. Petrov, D. Y. Prokhorov, V.M. Korzhavin, Lithium divertor concepts and results of supporting experiments, Plasma Phys. Controlled Fusion 44 (2002) 955–977.

[3] R. Kaita, R. Majeski, T. Gray, H. Kugel, D. Mansfield, J. Spaleta, J. Timberlake, L. Zakharov, Low recycling and high power density handling physics in the current drive experiment-upgrade with lithium plasma-facing components, Phys. Plasmas 14 (2007), 056111.

[4] Q. Yang, Z. Chen, Q. Du, H. Xu, G. Zuo, J. Ren, J. Hu, Y. Song, J. Li, F. Ding, L. Zakharov, Development of the flowing liquid lithium limiter for east tokamak, Fusion Eng. Des. 124 (2017) 179–182.

[5] A. Vertkov, I. Lyublinski, M. Zharkov, G. Mazzitelli, M.L. Apicella, Liquid tin limiter for ftu tokamak, Fusion Eng. Des. 117 (2017) 130–134.

[6] I.R. Kirillov, E.V. Muraviev, Review of liquid metal divertor concepts for tokamak reactors, Fusion Technol. (1996) 251–254.

[7] M.A. Abdou, T.A. TEAM, A. Ying, N. Morley, K. Gulec, S. Smolentsev, M. Kotschenreuther, S. Malang, S. Zinkle, T. Rognlien, P. Fogarty, B. Nelson, R. Nygren, K. McCarthy, M.Z. Youssef, N. Ghoniem, D. Sze, C. Wong, M. Sawan, H. Khater, R. Wooley, R. Mattas, R. Moir, S. Sharafat, J. Brooks, A. Hassanein, D. Petti, M. Tillack, M. Ulrickson, T. Uchimoto, On the exploration of innovative concepts for fusion chamber technology, Fusion Eng. Design 54 (2001) 181–247.

[8] R.E. Nygren, T.D. Rognlien, T.D. Rensink, S.S. Smolentsev, M.Z. Youssef, M. E. Sawan, B.J. Merrill, C. Eberle, P.J. Fogarty, B.E. Nelson, D.K. Sze, R. Majeski, A fusion reactor design with a liquid first wall and divertor, Fusion Eng. Des. 72 (2004) 181–221.

[9] R.E. Nygren, F.L. Tabarés, Liquid surfaces for plasma facing components—a critical review. Part i: physics and psi, Nucl. Mater. Energy 9 (2016) 6–21.

[10] M. Jaworski, T. Abrams, J. Allain, M. Bell, R. Bell, A. Diallo, T. Gray, S. Gerhardt, R. Kaita, H. Kugel, B. LeBlanc, R. Maingi, A. McLean, J. Menard, R. Nygren, M. Ono, M. Podesta, A. Roquemore, S. Sabbagh, F. Scotti, C. Skinner, V. Soukhanovskii, D. Stotler, the NSTX Team, Liquid lithium divertor characteristics and plasma–material interactions in nstx high-performance plasmas, Nucl. Fusion 53 (2013), 083032.

[11] D.K. Mansfield, K.W. Hill, J.D. Strachan, M.G. Bell, S.D. Scott, R. Budny, E.S. Marmar, J.A. Snipes, J.L. Terry, S. Batha, R.E. Bell, M. Bitter, C.E. Bush, Z. Chang, D.S. Darrow, D. Ernst, E. Fredrickson, B. Grek, H.W. Herrmann, A. Janos, D.L. Jassby, F.C. Jobes, D.W. Johnson, L.C. Johnson, F.M. Levinton, D.R. Mikkelsen, D. Mueller, D.K. Owens, H. Park, A.T. Ramsey, A.L. Roguemore, C.H. Skinner, T. Stevenson, B.C. Stratton, E. Synakowski, G. Taylor, A. von Halle, S. von Goeler, K.L. Wong, S.J. Zweben, T. Group, Enhancement of tokamak fusion test reactor performance by lithium conditioning, Phys. Plasmas 3 (1996) 1892.

[12] R. Majeski, T. Abrams, D. Boyle, E. Granstedt, J. Hare, C.M. Jacobson, R. Kaita, T. Kozub, B. LeBlanc, D.P. Lundberg, M. Lucia, E. Merino, J. Schmitt, D. Stotler, T.M. Biewer, J.M. Canik, T.K. Gray, R. Maingi, A.G. McLean, S. Kubota, W.A. Peebles, P. Beiersdorfer, J.H.T.C. an K. Tritz, Particle control and plasma performance in the lithium tokamak experiment, Phys. Plasmas 20 (2013) 056103.

[13] L.E. Zakharov, On a burning plasma low recycling regime with p_{DT}= 23–26mw, q_{DT}= 5–7 in a jet-like tokamak, Nucl. Fusion 59 (2019), 096008.

[14] M.G. Hvasta, E. Kolemen, A.E. Fisher, H. Ji, Demonstrating electromagnetic control of free-surface, liquid-metal flows relevant to fusion reactors, Nucl. Fusion 58 (2018), 016022.

[15] N.B. Morley, S. Smolentsev, D. Gao, Modeling infinite/axisymmetric liquid metal magnetohydrodynamic free surface flows, Fusion Eng. Des. 63–64 (2002) 343–351.

[16] E. Kolemen, M.G. Hvasta, R. Majeski, R. Maingi, A. Brooks, T. Kozub, Design of flowing liquid torus (flit), Nucl. Mater. Energy 19 (2019) 524–530.

[17] P. Fiflis, L. Kirsch, D. Andruczyk, D. Curreli, D.N. Ruzic, Seebeck coefficient measurements on li, sn, ta, mo, and w, J. Nucl. Mater. 438 (2013) 224–227.

[18] D.N. Ruzic, W. Xu, D. Andruczyk, M.A. Jaworski, Lithium-metal infused trenches (limit) for heat removal in fusion devices, Nucl. Fusion 51 (2011), 102002.

[19] M. Shimada, Y. Hirooka, Actively convected liquid metal divertor, Nucl. Fusion 54 (2014), 122002.

[20] D.N. Ruzic, M. Szott, C. Sandoval, M. Christenson, P. Fiflis, S. Hammouti, K. Kalathiparambil, I. Shchelkanov, D. Andruczyk, R. Stubbers, C.J. Foster, B. Jurczyk, Flowing liquid lithium plasma-facing components – physics, technology and system analysis of the limit system, Magnetohydrodynamics 12 (2017) 1324–1329.

[21] L.G. Golubchikov, V.A. Evtikhin, I.E. Lyublinski, V.I. Pistunovich, I.N. Potapov, A. N. Chumanov, Development of a liquid-metal fusion reactor divertor with a capillary-pore system, J. Nucl. Mater. 233–237 (1996) 667–672.

[22] V.A. Evtikhin, I.E. Lyublinski, A.V. Vertkov, N.I. Yezhov, B.I. Khripunov, S. M. Sotnikov, S.V. Mirnov, V.B. Petrov, Energy removal and mhd performance of lithium capillary-pore systems for divertor target application, Fusion Eng. Des. 49–50 (2000) 195–199.

[23] V.V. Buryak, A.A. Kolesnichenko, A.F. Kolesnichenko, S. Smolentsev, Free-surface mhd flows as a potential tool for high heat flux removal in fusion applications, Magnetohydrodynamics 48 (2012) 651–666.

[24] H.W. Davison, Compilation of thermophysical properties of liquid lithium (Technical Report), National Aeronautics and Space Administration, 1968.

[25] M. Pokorny, H.U. Åström, Temperature dependence of the electrical resistivity of liquid tin between 214 degrees c and 705 degrees c, J. Phys. F: Met. Phys. 5 (1975) 1327–1332.

[26] M.J. Assael, A.E. Kalyva, K.D. Antoniadis, R.M. Banish, I. Egry, J. Wu, E. Kaschnitz, W.A. Wakeham, Reference data for the density and viscosity of liquid copper and liquid tin, J. Phys. Chem. Ref. Data 39 (2010), 033105.

[27] P.W. Humrickhouse, An equation of state and compendium of thermophysical properties of liquid tin, a prospective plasma-facing material, IEEE Trans. Plasma Sci. 47 (2019) 3374–3379.

[28] F. Arbeiter, Y. Chen, B.-E. Ghidersa, C. Klein, H. Neuberger, S. Ruck, G. Schlindwein, F. Schwab, A. von der Weth, Options for a high heat flux enabled helium cooled first wall for demo, Fusion Eng. Des. 119 (2017) 22–28.

[29] J.C.R. Hunt, Magnetohydrodynamic flow in rectangular ducts, J. Fluid Mech. 21 (1967) 577–590.

[30] K. Miyazaki, S. Inoue, N. Yamaoka, T. Horiba, K. Yokomizo, Magneto-hydro-dynamic pressure drop of lithium flow in rectangular ducts, Fusion Technol. 10 (1986) 830–836.

[31] A.E. Fisher, E. Kolemen, M.G. Hvasta, Experimental demonstration of hydraulic jump control in liquid metal channel flow using lorentz force, Phys. Fluids 30 (2018), 067104.

[32] M.G. Hvasta, E. Kolemen, A. Fisher, Application of ir imaging for free-surface velocity measurement in liquid-metal systems, Rev. Sci. Instrum. 88 (2017), 013501.

[33] A.E. Fisher, M.G. Hvasta, E. Kolemen, Study of liquid metal surface wave damping in the presence of magnetic fields and electrical currents, Nucl. Mater. Energy 19 (2019) 101–106.

[34] COMSOL, CFD Module User's Guide, comsol multiphysics 5.4 edition, 2018.

[35] COMSOL, AC/DC Module User's Guide, comsol multiphysics 5.4 edition, 2018.

[36] COMSOL, COMSOL Multiphysics Reference Manual, comsol multiphysics 5.4 edition, 2018.

[37] V.H. Gada, A. Sharma, On derivation and physical interpretation of level set method-based equations for two-phase flow simulations, Numer. Heat Transfer Part B: Fundamentals 56 (2009) 307–322.